Black holes immersed in modified Chaplygin-like dark fluid and cloud of strings: shadows, quasinormal modes, and greybody factors*

Hao-Peng Yan (闫浩鹏)[†]   Zeng-Yi Zhang (张增益)   Xiao-Jun Yue (岳晓军)   Xiang-Qian Li (李向前)[‡]

College of Physics and Optoelectronic Engineering, Taiyuan University of Technology, Taiyuan 030024, China

Abstract: We present a unified investigation of black hole shadows, quasinormal modes (QNMs), and greybody factors (GBFs) for a static, spherically symmetric black hole within a composite environment of a modified Chaplygin-like dark fluid (MCDF) and a cloud of strings (CoS). We examine the structure of critical photon orbits and the corresponding optical appearance under spherical accretion. Using the Wentzel–Kramers–Brillouin (WKB) approximation, we compute the quasinormal frequencies and greybody spectra and explore their correspondence with the black hole shadows in the eikonal limit. A systematic parameter study demonstrates that the CoS intensity has the primary influence on the shadows, QNMs, and GBFs, whereas the MCDF parameters introduce more complex but characterizable modifications to each. Our results demonstrate that these environmental components imprint distinct yet interrelated signatures on key observables, offering specific predictions for probing exotic black hole environments.

Keywords: modified Chaplygin-like dark fluid, cloud of strings, black hole shadow, quasinormal modes, greybody factors

I. INTRODUCTION

The existence of black holes, once a purely theoretical prediction of general relativity, is now firmly established by astronomical observations. The landmark images of the supermassive black holes M87* and Sgr A* obtained by the Event Horizon Telescope collaboration have inaugurated a new era of strong-field gravity astronomy, wherein the black hole shadow provides a direct probe of spacetime geometry in the immediate vicinity of the event horizon [1, 2]. Concurrently, the advent of gravitational wave astronomy has opened a complementary observational window into the dynamics of compact objects, with the ringdown phase characterized by quasinormal modes (QNMs) —complex-frequency oscillations that constitute unique gravitational wave fingerprints of black holes [3, 4].

These observational breakthroughs demand a deeper theoretical understanding of black holes in environments that more realistically reflect their cosmological context. To this end, three principal theoretical tools have emerged as crucial diagnostics of black hole structure and dynamics. Black hole shadows characterize the optical appearance through critical photon orbits [5−24]. Recent explorations have expanded this framework to diverse environments [25−29], with contemporary studies even investigating the intriguing possibility of using shadows as novel probes for particle dark matter [30]. QNMs reveal the stability and characteristic ringing of spacetime under external perturbations [31−39]. Greybody factors (GBFs) govern the transmission probability of Hawking radiation to distant observers, providing essential insights into semi-classical evaporation processes and quantum effects in curved spacetime [40−42].

Furthermore, recent studies have revealed profound physical connections among these three diagnostics, establishing a rigorous framework for probing strong-field gravity. In the eikonal limit, a well-established correspondence links QNM frequencies to the properties of the photon sphere and consequently to the shadow radius [43−49]. Complementing this geometric picture, a recent study has demonstrated that the GBF plays a pivotal role in governing the excitation amplitude of the ringdown signal, thereby directly linking transmission probabilities to gravitational wave observables [50]. Concurrently, observations suggest that greybody spectra often exhibit

---

greater robustness than quasinormal frequencies under small perturbations of the geometry, offering a complementary diagnostic for the near-horizon structure [51, 52]. More broadly, the scattering interpretation has been deepened to explicitly connect quasinormal frequencies with the transmission and reflection coefficients of the effective potential [53, 54]. This multifaceted correspondence between geometry (shadow), dynamics (QNMs), and scattering (GBFs) now serves as a concrete paradigm for synergistically analyzing black hole physics across different observational channels [55−58].

The application of these tools becomes particularly significant in the context of modern cosmology, where dark energy and dark matter dominate the energy content [59, 60]. Among various proposals, quintessence dark energy offers a compelling explanation for cosmic acceleration [61, 62]. The foundational work by Kiselev, who first derived a static, spherically symmetric black hole solution surrounded by quintessence matter [63], established a framework for studying how dark energy influences black hole shadows [29, 64−67], QNMs, and GBFs [25, 68−70]. Unified models that simultaneously describe dark matter and dark energy have attracted significant attention, among which the Chaplygin gas [71] and its generalizations stand as prominent candidates. These models successfully account for diverse cosmological observations [71−75]. Notably, the Chaplygin gas emerges naturally within string theory frameworks, transcending its purely phenomenological origins [76−78]. Black holes immersed in Chaplygin-like dark fluids—including the original Chaplygin-like dark fluid (CDF), its generalized extension (GCDF), and a modified version (MCDF)—have been extensively studied [79−87].

Further enriching this landscape, the cloud of strings (CoS) model provides a minimalist geometric framework for describing how one-dimensional extended objects can modify black hole spacetimes. Originally developed by Letelier [88], this model generalizes the concept of a dust cloud to a collection of one-dimensional strings. Physically, it can be interpreted as a macroscopic effective description of topological defects—analogous to cosmic strings—formed during symmetry-breaking phase transitions in the early universe. While not intended to model standard astrophysical accretion flows (such as gas or dust), the CoS serves as a valuable toy model for investigating the gravitational imprints of global anisotropy and extended structures. By treating the background as a continuous fluid with string-like stress, this framework allows one to isolate and study how remnant networks of primordial defects might modify the classical observables in strong-field gravity, distinct from point-particle matter distributions. Recently, studies of black holes immersed in a CoS have attracted growing interest [28, 67, 89−92].

Building upon a previous study [84], which investig-

ated timelike and null geodesics, shadows, and images of MCDF-CoS black holes surrounded by thin accretion disks, the present study extends this analysis to encompass the QNM spectrum and GBFs, while systematically exploring the fundamental relationships among the black hole shadow, QNMs, and GBFs within this framework.

The remainder of this paper is structured as follows. Section II introduces a static, spherically symmetric black hole solution immersed in both an MCDF and a CoS. Section III analyzes critical photon orbits and the black hole shadow, alongside optical appearances under spherical accretion. Section IV presents QNM computations and discusses their physical implications. Section V examines GBFs and their parameter dependence. Finally, Section VI summarizes our principal findings and discusses their broader implications.

II. BLACK HOLE IMMERSED IN A MODIFIED CHAPLYGIN-LIKE DARK FLUID AND A CLOUD OF STRINGS

We consider a static, spherically symmetric spacetime metric describing a black hole immersed in both an MCDF and a CoS. The line element takes the form [84]

$$ds^2 = -f(r)dt^2 + \frac{1}{f(r)}dr^2 + r^2d\Omega^2, \tag{1}$$

where $d\Omega^2 = d\theta^2 + \sin^2\theta d\phi^2$ represents the metric on the two-sphere, and $f(r)$ denotes the lapse function

$$f(r) = 1 - \frac{2M}{r} - a + G(r). \tag{2}$$

Here, a parameterizes the CoS contribution, and $G(r)$ encapsulates the MCDF influence, explicitly given by

$$G(r) = -\frac{r^2}{3}\left(\frac{1+A}{B}\right)^{a_1} {}_2F_1[a_1, a_2; a_3; a_4], \tag{3}$$

where ${}_2F_1[a_1, a_2; a_3; a_4]$ is the Gauss hypergeometric function with parameters defined as

$$a_1 = -(1+\beta)^{-1}, \tag{4}$$

$$a_2 = a_1(1+A)^{-1}, \tag{5}$$

$$a_3 = 1 + a_2, \tag{6}$$

$$a_4 = -B^{-1}Q^{-3/a_2}r^{3/a_2}. \tag{7}$$

The parameters $A \geq 0$, $B > 0$, and $0 \leq \beta \leq 1$ specify the equation of state of the MCDF [73, 81] as follows:

$$p = A\rho - \frac{B}{\rho^\beta}, \tag{8}$$

with $Q > 0$ representing the MCDF intensity. This model provides a unified description of dark matter and dark energy [71, 72]. In the limit $A = 0$, Eq. (8) reduces to the generalized Chaplygin gas form, $p = -B/\rho^\beta$ [73]; further setting $\beta = 1$ recovers the original Chaplygin gas form, $p = -B/\rho$ [71].

The asymptotic behavior of the lapse function, illustrated in Fig. 1 and discussed in Ref. [84, 85], reveals that, as $r \to \infty$,

$$f(r) \to 1 - a - \frac{r^2}{3}\left(\frac{1+A}{B}\right)^{-\frac{1}{1+\beta}}. \tag{9}$$

This indicates that the spacetime is asymptotically de Sitter, with an effective cosmological constant shaped by the MCDF parameters:

$$\Lambda_{\mathrm{MCDF}} \equiv \left(\frac{1+A}{B}\right)^{-\frac{1}{1+\beta}}. \tag{10}$$

However, this metric describes a black hole only within specific parameter ranges that ensure the existence of event horizons. As shown in Fig. 1 and subsequent analysis, black hole solutions require upper bounds on a, B, and Q and lower bounds on A and β. Our analysis is accordingly restricted to such physical parameter regions. For such asymptotically de Sitter black hole spacetimes, both an event horizon r_h and a cosmological horizon r_c exist, corresponding to roots of $f(r)$. Additionally, a Cauchy horizon appears inside the black hole whenever the MCDF intensity Q is nonzero.

When $a = 0$, the black hole metric (1) describes a black hole immersed solely in an MCDF. In the limit $Q \to 0$, the MCDF lapse function reduces to

$$f(r) \to 1 - \frac{2M}{r} - \frac{r^2}{3}\Lambda_{\mathrm{MCDF}}, \tag{11}$$

which describes a Schwarzschild-de Sitter (S-dS) black hole upon identifying the effective cosmological constant Λ_{MCDF} [Eq. (10)] with the standard cosmological constant Λ. This connection highlights the role of the MCDF in driving cosmic acceleration. The specific cases of $(A = 0, \beta \neq 1)$ and $(A = 0, \beta = 1)$ yield the GCDF and CDF black hole metrics, respectively. Note that, while Λ_{MCDF} fixes the large-r asymptotic structure, the parameter A predominantly influences the near-horizon geometry and the precise location of the event horizon, particularly for

small values of A.

In subsequent analysis, we set $M = 1$ for computational convenience.

III. SHADOW AND OPTICAL APPEARANCE

A. Critical photon orbits and black hole shadow

The propagation of null geodesics with energy E and angular momentum L is governed by [84]

$$\dot{t} = \frac{E}{f(r)}, \tag{12}$$

$$\dot{\phi} = \frac{L}{r^2}, \tag{13}$$

$$\dot{r}^2 + \mathcal{V}(r) = E^2, \tag{14}$$

where dots denote derivatives with respect to the affine parameter s, and

$$\mathcal{V}(r) = \frac{L^2}{r^2}f(r) \tag{15}$$

is the effective potential for radial motion. The explicit energy dependence can be scaled out, reducing the photon trajectory description to a single parameter: the impact parameter $b \equiv L/E$.

The photon sphere radius, comprising unstable spherical photon orbits, is determined by

$$f(r_{\mathrm{ps}}) - \frac{1}{2}r_{\mathrm{ps}}f'(r_{\mathrm{ps}}) = 0, \tag{16}$$

where primes indicate radial derivatives. The corresponding critical impact parameter and angular velocity are

$$b_{\mathrm{ps}} = \frac{r_{\mathrm{ps}}}{\sqrt{f(r_{\mathrm{ps}})}}, \tag{17}$$

$$\Omega_{\mathrm{ps}} = \frac{\sqrt{f(r_{\mathrm{ps}})}}{r_{\mathrm{ps}}}, \tag{18}$$

whereas the Lyapunov exponent, characterizing orbital instability, is given by

$$\lambda = \frac{1}{\sqrt{2}}\sqrt{\frac{f(r)}{r^2}\left(2f(r) - r^2 f''(r)\right)}\bigg|_{r=r_{\mathrm{ps}}}. \tag{19}$$

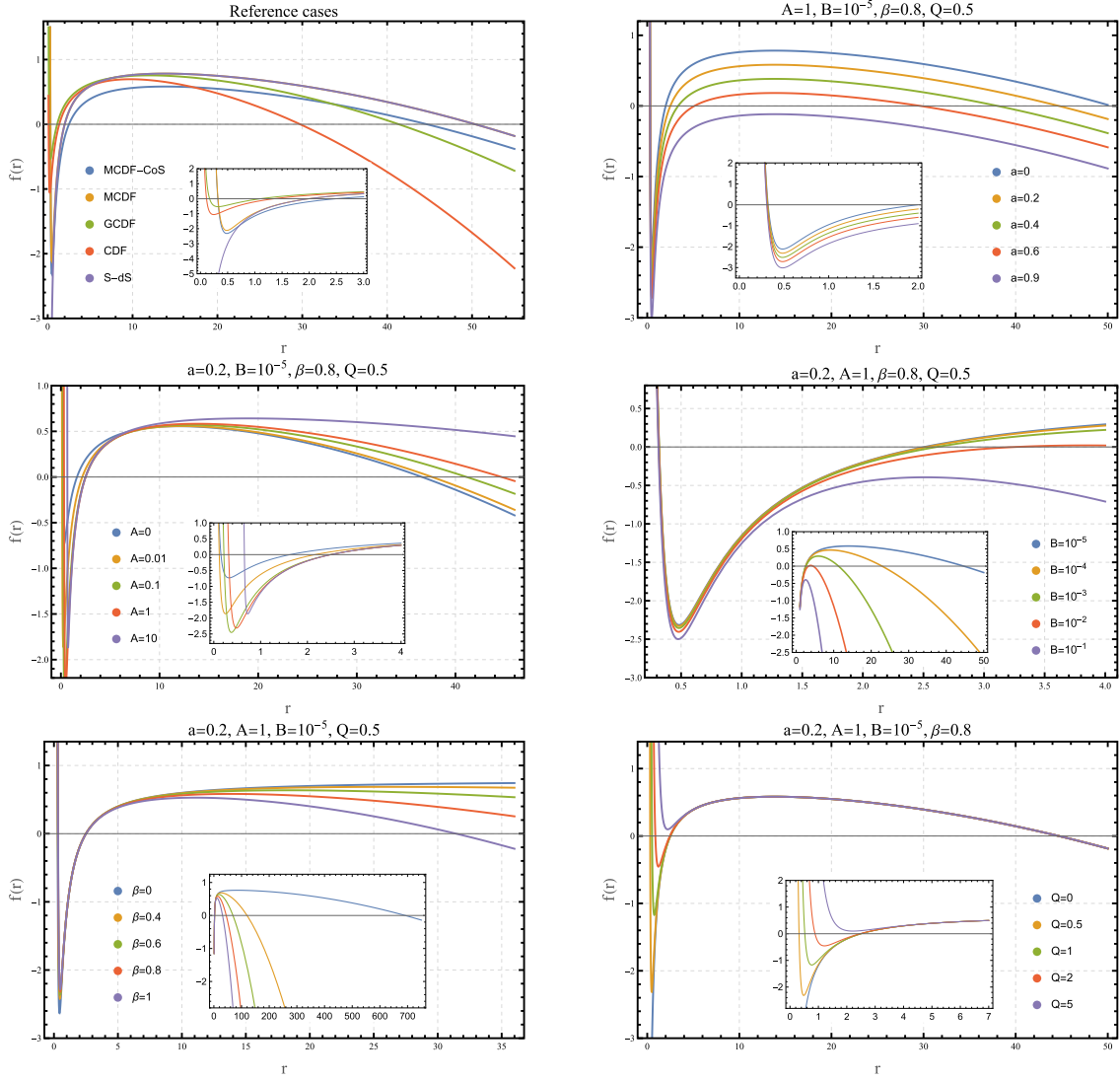For a distant observer at r_O, the shadow radius becomes

Fig. 1. (color online) Lapse function $f(r)$ for diverse parameter configurations. The first panel displays an MCDF-CoS reference case with $a = 0.2$, $A = 1$, $B = 10^{-5}$, $\beta = 0.8$, and $Q = 0.5$, alongside specific limits: MCDF ($a = 0$), GCDF ($a = 0$, $A = 0$, $\beta \neq 1$), CDF ($a = 0$, $A = 0$, $\beta = 1$), and Schwarzschild-de Sitter ($a = 0$, $Q = 0$). Subsequent panels show varying individual parameters, while others are maintained at reference values.

$$R_s = b_{\mathrm{ps}} \sqrt{f(r_O)}. \qquad (20)$$

B.   Optical appearance under spherical accretion

While previous studies examined MCDF-CoS black holes with thin accretion disks [84], we focus on spherical accretion models. The specific intensity observed at $r = r_O$ is given by [93, 94]

$$I = \int_\gamma g^3 j(\nu_\mathrm{e}) \mathrm{d}l_\mathrm{p}, \qquad (21)$$

where $g = \nu_o/\nu_\mathrm{e}$ is the redshift factor, $j(\nu_\mathrm{e})$ is the emissivity per unit volume in the emitter's frame, $\mathrm{d}l_\mathrm{p}$ is the infin-

itesimal proper length, and γ is the light ray trajectory.

1.   *Static accretion model*

For static spherical accretion, $g = [f(r)/f(r_O)]^{1/2}$. Assuming monochromatic emission at frequency ν_s, the specific emissivity follows:

$$j(\nu_e) \propto \delta(\nu_e - \nu_s) r^{-m}, \qquad (22)$$

where we adopt $m = 2$ following established conventions [94], although $m = 4$ [6] and $m = 6$ [95] are also physically motivated. The proper length element is

$$dl_{\mathrm{p}} = \sqrt{f(r)^{-1}dr^2 + r^2 d\phi^2} = \sqrt{f(r)^{-1} + r^2 \left(\frac{d\phi}{dr}\right)^2}\, dr, \quad (23)$$

with $d\phi/dr$ derivable from Eqs. (13) and (14). The observed specific intensity thus becomes

$$I_{\mathrm{obs}} = \int_\gamma \left[\frac{f(r)}{f(r_{\mathrm{O}})}\right]^{3/2} r^{-2} \sqrt{f(r)^{-1} + r^2 \left(\frac{d\phi}{dr}\right)^2}\, dr. \quad (24)$$

2. Infalling accretion model

For infalling accretion, the redshift factor incorporates flow velocity effects as follows:

$$g = \frac{k_\beta u_{\mathrm{O}}^\beta}{k_\gamma u_{\mathrm{e}}^\gamma}, \quad (25)$$

where $k^\mu = \dot{x}_\mu$ is the photon four-velocity, $u_{\mathrm{O}}^\mu = (f(r_{\mathrm{O}})^{-1/2}, 0, 0, 0)$ is the four-velocity of the static observer, and

$$u_{\mathrm{e}}^t = \frac{1}{f(r)}, \quad u_{\mathrm{e}}^r = -\sqrt{1 - f(r)}, \quad u_{\mathrm{e}}^\theta = u_{\mathrm{e}}^\phi = 0, \quad (26)$$

is the accretion flow four-velocity. For null geodesics with affine parameter $s \to s/|L|$, $k_t = 1/b$ remains constant, whereas k_r follows from $k_\alpha k^\alpha = 0$:

$$\frac{k_r}{k_t} = \pm \frac{1}{f(r)} \sqrt{1 - \frac{b^2 f(r)}{r^2}}, \quad (27)$$

with signs distinguishing between incoming $(-)$ and outgoing $(+)$ photons. This yields the simplified redshift factor

$$g = \frac{1}{u_{\mathrm{e}}^t + (k_r/k_t) u_{\mathrm{e}}^r}, \quad (28)$$

which differs fundamentally from the static case.

The proper distance becomes

$$dl_{\mathrm{p}} = k_\mu u_{\mathrm{e}}^\mu ds = \frac{k_t}{g|k_r|} dr, \quad (29)$$

leading to the observed intensity

$$I_{\mathrm{obs}} \propto \int_\gamma \frac{g^3 k_t dr}{r^2 |k_r|}. \quad (30)$$

We employ $f(r_{\mathrm{O}})^{3/2} I_{\mathrm{obs}}(b)$ for numerical analysis to remove the observer-position dependence. The absolute value $|k_r|$ accounts for photon direction reversals along the trajectory.

3. Optical appearance analysis

Our analysis of the optical appearance of the MCDF-CoS black hole, based on the numerical integration of specific intensities for static (Eq. (24)) and infalling (Eq. (30)) accretion models, reveals characteristic features. The observed intensity $f(r_{\mathrm{O}})^{3/2} I_{\mathrm{obs}}(b)$, plotted against impact parameter b in Figs. 2 and 3, exhibits a universal profile: intensity rises sharply with b, peaks at the photon sphere $b = b_{\mathrm{ps}}$, and then declines rapidly. This defines the black hole shadow—a central dark region ($b < b_{\mathrm{ps}}$) where most photons are absorbed by the event horizon. The intensity maximum at b_{ps} results from photons undergoing multiple unstable orbits, accumulating enhanced path lengths through the emitting medium. For $b > b_{\mathrm{ps}}$, intensity derives from refracted rays and diminishes with increasing b.

Despite sharing the identical shadow radius $b_{\mathrm{ps}} \sqrt{f(r_O)}$ (a geometric invariant), the two accretion models produce distinct observational signatures. Static accretion yields a sharper, narrower, brighter emission ring, whereas infalling accretion generates a broader, fainter ring with a darker shadow interior. This suppression in the infalling case manifests Doppler beaming: radially infalling matter redshifts forward-emitted radiation, reducing the detected flux at infinity.

Parameter variations systematically affect the shadow and emission ring. The CoS parameter a exerts the strongest influence: increasing a significantly enlarges the shadow radius while reducing intensity. The MCDF parameters produce more nuanced effects: Q has a negligible impact; decreasing β slightly enhances intensity without affecting the shadow radius; only extreme A and B values noticeably alter the images. Specifically, increasing A enlarges the shadow and reduces intensity (both effects saturating at large A), whereas increasing B reduces both shadow size and intensity. These consistent trends across accretion models confirm that spacetime geometry primarily determines shadow properties, whereas accretion dynamics shape the bright ring characteristics.

IV. QUASINORMAL MODES

We investigate the propagation of a massless scalar field on the fixed background of the MCDF-CoS black hole spacetime, described by the metric in Eq. (1). The dynamics of the scalar perturbation are governed by the covariant Klein-Gordon equation [31, 32] given as follows:

$$\nabla_\mu \nabla^\mu \Phi = \frac{1}{\sqrt{-g}} \partial_\mu \left(\sqrt{-g} g^{\mu\nu} \partial_\nu \Phi\right) = 0. \quad (31)$$

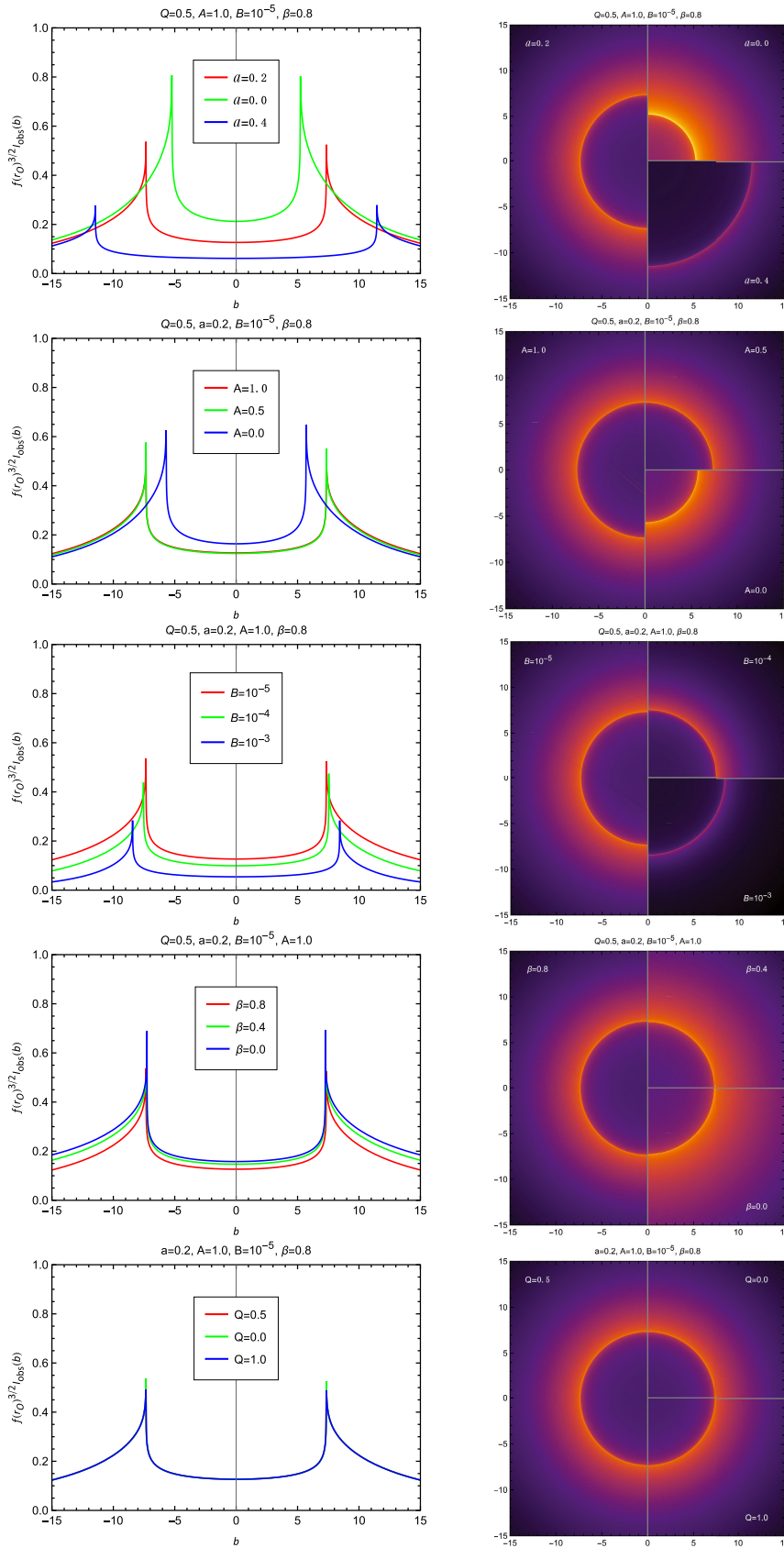Owing to the spherical symmetry of the background, the

Fig. 2. (color online) Profiles of the specific intensity $I_{\text{obs}}(b)$ (left panels) and corresponding images (right panels) for static spherical accretion, viewed face-on by an observer near the pseudo-cosmological horizon
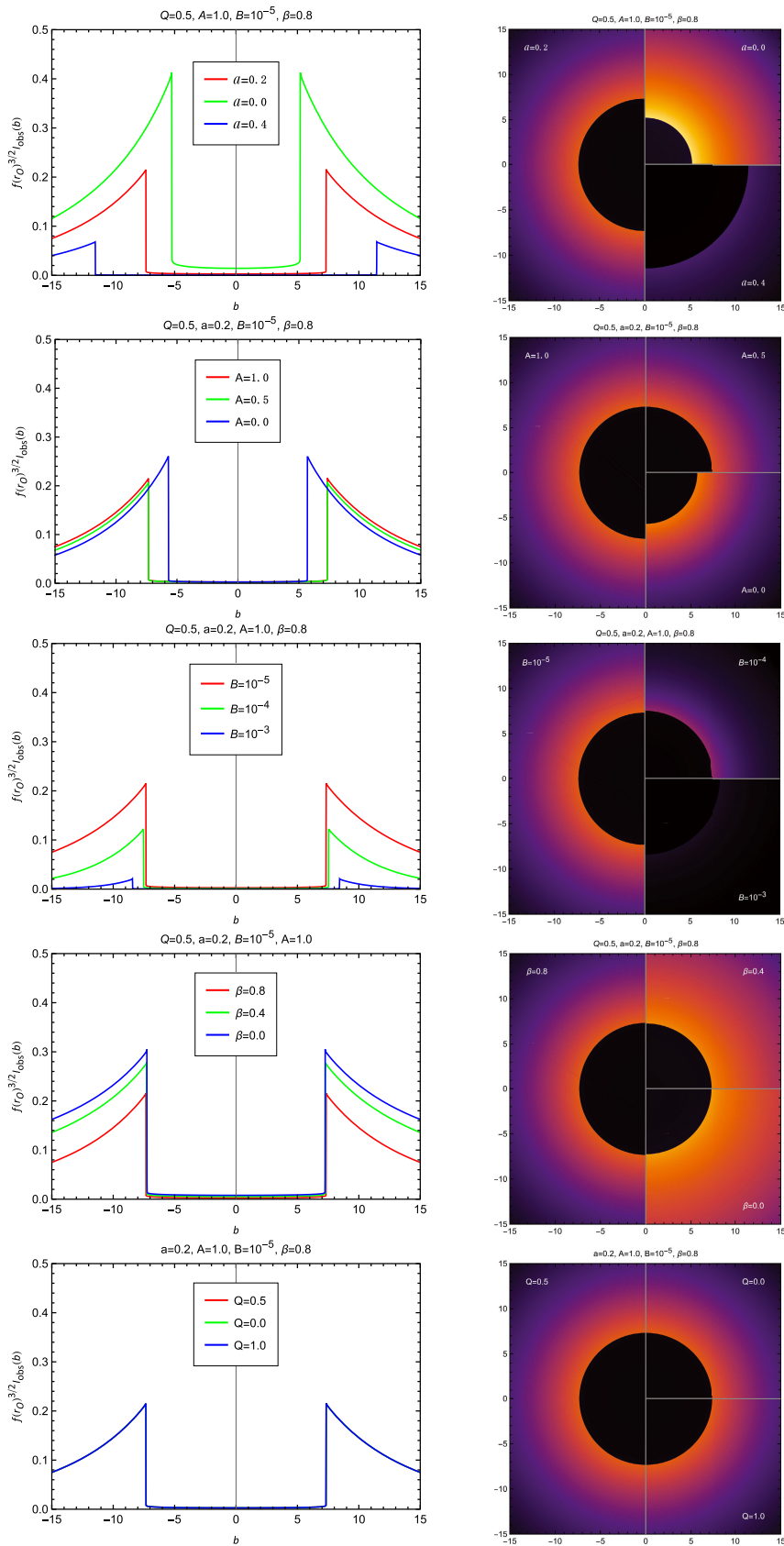
Fig. 3. (color online) Profiles of the specific intensity $I_{obs}(b)$ (left panels) and corresponding images (right panels) for infalling spherical accretion, viewed face-on by an observer near the pseudo-cosmological horizon

field equation admits the separation of variables via the ansatz

$$\Phi(t, r, \theta, \phi) = \frac{\Psi(r)}{r} Y_{\rm lm}(\theta, \phi) e^{-i\omega t}, \tag{32}$$

where $Y_{\rm lm}(\theta, \phi)$ are the standard spherical harmonics, and ω is the complex QNM frequency. The real part, ω_R, corresponds to the oscillation frequency, whereas the imaginary part, ω_I, determines the damping rate. Substituting this ansatz into Eq. (31) leads to a Schrödinger-like wave equation for the radial function $\Psi(r)$

$$\frac{{\rm d}^2\Psi}{{\rm d}r_*^2} + \left[\omega^2 - V(r)\right]\Psi = 0, \tag{33}$$

governed by the effective potential

$$V(r) = f(r)\left[\frac{l(l+1)}{r^2} + \frac{1}{r}\frac{{\rm d}f(r)}{{\rm d}r}\right]. \tag{34}$$

Here, the tortoise coordinate r_* is defined by

$$\mathrm{d}r_* = \frac{\mathrm{d}r}{f(r)}, \tag{35}$$

which maps the event horizon r_h and cosmological horizon r_c to $r_* \to -\infty$ and $r_* \to +\infty$, respectively, ensuring that $V(r) \to 0$ at both boundaries.

The QNM spectrum consists of discrete complex eigenvalues $\{\omega_n\}$, which are determined by imposing purely outgoing wave boundary conditions at both horizons:

$$\Psi(r_*) \sim e^{-i\omega r_*} \quad \text{as} \quad r_* \to -\infty \quad (\text{near } r_h), \tag{36}$$

$$\Psi(r_*) \sim e^{+i\omega r_*} \quad \text{as} \quad r_* \to +\infty \quad (\text{near } r_c). \tag{37}$$

These boundary conditions render the eigenvalue problem non-self-adjoint, leading to a discrete set of complex frequencies $\omega = \omega_R + i\omega_I$ that encode the intrinsic, model-dependent ringing of the spacetime.

A. Computational methods

To compute the QNM frequencies, we employ two complementary semi-analytical techniques that are well-suited for effective potentials with a single maximum: the higher-order WKB approximation and the Mashhoon method.

The WKB method, originally adapted from quantum mechanics for the black hole perturbation theory [96], has been systematically developed to high orders [54, 97, 98]. This technique matches asymptotic solutions across the

turning points of the potential via a Taylor expansion around its maximum r_*^0. The foundational third-order WKB formula is given by [97]

$$\omega^2 = V_0 + \sqrt{-2V_0^{(2)}}\,\Lambda_2(\mathcal{K}) - i\mathcal{K}\sqrt{-2V_0^{(2)}}\,[1 + \Lambda_3(\mathcal{K})], \tag{38}$$

where V_0 is the maximum potential value, $V_0^{(2)}$ is its second derivative at r_*^0, $\mathcal{K} = n + 1/2$ is the overtone number, and Λ_2 and Λ_3 are polynomials incorporating higher-order WKB corrections [97]. This method provides high accuracy for fundamental modes ($n = 0$) with $l > n$, and its precision improves with increasing angular momentum l.

The Mashhoon method [99, 100] offers an alternative, more intuitive approach by approximating the effective potential with the exactly solvable Pöschl-Teller potential

$$V_{\rm P\text{-}T}(r_*) = \frac{V_0}{\cosh^2[\alpha(r_* - r_*^0)]}, \tag{39}$$

where the parameter α is determined by the curvature of the potential at its maximum: $\alpha^2 = -\frac{1}{2V_0}\frac{{\rm d}^2 V}{{\rm d}r_*^2}\big|_{r_* = r_*^0}$. This approximation yields an analytical expression for the QNM frequencies,

$$\omega_{\rm P\text{-}T} = \sqrt{V_0 - \frac{\alpha^2}{4}} - i\alpha\left(n + \frac{1}{2}\right). \tag{40}$$

While generally less accurate than the higher-order WKB method for quantitative predictions, the Mashhoon method is highly effective for capturing qualitative trends and verifying parameter dependencies.

B. Eikonal correspondence and shadow relationship

In the eikonal limit ($l \gg 1$), a profound correspondence emerges between the wave dynamics of QNMs and the geometric properties of null geodesics [43]. In this regime, the effective potential (Eq. (34)) simplifies to $V_{\rm eik}(r) \approx f(r)l^2/r^2$, which relates directly to the null geodesic potential (Eq. (15)), and its maximum coincides with the location of the unstable photon sphere. The QNM frequencies are then directly linked to the characteristics of null geodesics orbiting the photon sphere: $\omega_{\rm eik} \approx \omega_{\rm PS}$, where

$$\omega_{\rm PS} = \Omega_{\rm ps}l - i\left(n + \frac{1}{2}\right)|\lambda|, \tag{41}$$

$\Omega_{\rm ps}$ is the angular frequency of the photon orbits given by Eq. (18), and λ is the Lyapunov exponent, characterizing the instability timescale of these orbits, as defined in Eq. (19). This geometric correspondence extends further to

the black hole shadow observed by a distant observer. The real part of the QNM frequency is inversely related to the shadow radius R_s: $\mathrm{Re}(\omega_{\mathrm{eik}}) \approx l\sqrt{f(r_O)}/R_s$, where r_O is the radial coordinate of the observer. This fundamental connection between the wave and geometric descriptions provides a robust cross-check for our computations and deepens the physical interpretation of both QNMs and the black hole shadow.

C. QNM results and discussion

Our systematic analysis of MCDF-CoS QNMs, computed via the third-order WKB and Pöschl-Teller methods, is presented here (Tables 1–4, Figs. 4–6). The WKB approximation provides high accuracy for the fundamental modes ($n = 0$), particularly in the eikonal regime ($l > n$), but its precision deteriorates rapidly for higher

overtones ($n \geq 1$) [97, 98]. Consequently, we restrict our quantitative analysis to the fundamental mode ($n = 0$) and first overtone ($n = 1$), omitting higher harmonics ($n \geq 2$) where the method becomes unreliable. Generally, we observe strong correlations with the effective potential: higher barriers increase $\mathrm{Re}(\omega)$ (oscillation frequency), whereas broader barriers decrease $|\mathrm{Im}(\omega)|$ (damping rate).

The fundamental modes ($n = 0$, $l = 1$) across different configurations (see Table 1 and Fig. 4) exhibit high sensitivity to the matter content. The reference MCDF-CoS configuration shows substantially lower $\mathrm{Re}(\omega)$ compared with the GCDF or CDF cases, along with notable variations in the damping rate. This indicates the predominant nontrivial effect of the MCDF parameter A.

An analysis of parameter dependence reveals that the CoS parameter a exerts the strongest influence (Table 2, Fig. 5): increasing a monotonically reduces both $\mathrm{Re}(\omega)$

Table 1. Comparison of fundamental ($n = 0$, $l = 1$) QNM frequencies for different black hole models. The parameters for the reference MCDF-CoS case are $a = 0.2$, $A = 1$, $B = 10^{-5}$, $\beta = 0.8$, and $Q = 0.5$. The other cases represent specific limits of this general configuration. $\Delta_R\%$ and $\Delta_I\%$ denote the relative errors for the real and imaginary parts, respectively, calculated as $|\omega_{\mathrm{WKB}} - \omega_{\mathrm{P-T}}|/|\omega_{\mathrm{WKB}}| \times 100\%$.

Model	a	A	B	β	Q	ω_{WKB}	$\omega_{\mathrm{P-T}}$	$\Delta_R\%$	$\Delta_I\%$
MCDF-CoS	0.2	1	10^{-5}	0.8	0.5	0.203417 - 0.062029 i	0.207452 - 0.063452 i	1.96	2.29
MCDF	0	1	10^{-5}	0.8	0.5	0.289203 - 0.097471 i	0.296591 - 0.100235 i	2.56	2.84
GCDF	0	0	10^{-5}	0.8	0.5	0.417415 - 0.105700 i	0.422366 - 0.107314 i	1.19	1.53
CDF	0	0	10^{-5}	1	0.5	0.358448 - 0.096342 i	0.363282 - 0.098002 i	1.35	1.72
S-dS	0	1	10^{-5}	0.8	0	0.289352 - 0.097672 i	0.296573 - 0.100285 i	2.50	2.68

Table 2. Dependence of the fundamental ($n = 0$, $l = 1$) QNM frequencies on various metric parameters. Each section varies one parameter while maintaining others fixed at the reference values: $a = 0.2$, $A = 1$, $B = 10^{-5}$, $\beta = 0.8$, and $Q = 0.5$ (unless otherwise specified in the Fixed Parameters column). $\Delta_R\%$ and $\Delta_I\%$ denote the relative errors for the real and imaginary parts, respectively, calculated as $|\omega_{\mathrm{WKB}} - \omega_{\mathrm{P-T}}|/|\omega_{\mathrm{WKB}}| \times 100\%$.

Fixed Parameters	Variable Parameter	ω_{WKB}	$\omega_{\mathrm{P-T}}$	$\Delta_R\%$	$\Delta_I\%$
$Q = 0.5$ $A = 1.0$ $B = 10^{-5}$ $\beta = 0.8$	$a = 0.0$	0.289203 - 0.097471 i	0.296591 - 0.100235 i	2.56	2.84
	$a = 0.2$	0.203417 - 0.062029 i	0.207452 - 0.063452 i	1.96	2.29
	$a = 0.4$	0.128447 - 0.034367 i	0.130274 - 0.034983 i	1.42	1.79
$Q = 0.5$ $B = 10^{-5}$ $\beta = 0.8$ $a = 0.2$	$A = 0$	0.262068 - 0.062967 i	0.264851 - 0.063863 i	1.06	1.42
	$A = 0.5$	0.203224 - 0.061391 i	0.207297 - 0.062959 i	2.00	2.55
	$A = 1.0$	0.203417 - 0.062029 i	0.207452 - 0.063452 i	1.96	2.29
$Q = 0.5$ $A = 1$ $\beta = 0.8$ $a = 0.2$	$B = 10^{-5}$	0.203417 - 0.062029 i	0.207452 - 0.063452 i	1.96	2.29
	$B = 10^{-4}$	0.197131 - 0.060818 i	0.200639 - 0.062128 i	1.78	2.15
	$B = 10^{-3}$	0.173269 - 0.055551 i	0.175396 - 0.056418 i	1.23	1.56
$Q = 0.5$ $A = 1$ $B = 10^{-5}$ $a = 0.2$	$\beta = 0$	0.205887 - 0.062428 i	0.210128 - 0.063886 i	2.06	2.34
	$\beta = 0.4$	0.205472 - 0.062347 i	0.209709 - 0.063828 i	2.06	2.37
	$\beta = 0.8$	0.203417 - 0.062029 i	0.207452 - 0.063452 i	1.96	2.29
$A = 1$ $B = 10^{-5}$ $\beta = 0.8$ $a = 0.2$	$Q = 0$	0.203428 - 0.062043 i	0.207450 - 0.063458 i	1.96	2.28
	$Q = 0.5$	0.203417 - 0.062029 i	0.207452 - 0.063452 i	1.96	2.29
	$Q = 1$	0.203276 - 0.061806 i	0.207480 - 0.063383 i	2.07	2.55

Table 3. Dependence of QNM frequencies on the angular quantum number l and overtone number n for the reference black hole configuration: $a = 0.2$, $A = 1$, $B = 10^{-5}$, $\beta = 0.8$, and $Q = 0.5$. The analysis is restricted to the fundamental mode ($n = 0$) and first overtone ($n = 1$). $\Delta_R\%$ and $\Delta_I\%$ denote the relative errors for the real and imaginary parts, respectively, calculated as $|\omega_{\text{WKB}} - \omega_{\text{P-T}}|/|\omega_{\text{WKB}}| \times 100\%$.

l	n	ω_{WKB}	$\omega_{\text{P-T}}$	$\Delta_R\%$	$\Delta_I\%$
1	0	0.203417 - 0.062029 i	0.207452 - 0.063452 i	1.96	2.29
2	0	0.340450 - 0.061319 i	0.342732 - 0.061884 i	0.67	0.92
2	1	0.329178 - 0.186588 i	0.342732 - 0.185652 i	4.11	0.50
3	0	0.476940 - 0.061138 i	0.478537 - 0.061433 i	0.33	0.48
3	1	0.468668 - 0.184780 i	0.478537 - 0.184299 i	2.10	0.26
4	0	0.613332 - 0.061066 i	0.614562 - 0.061246 i	0.20	0.29
4	1	0.606829 - 0.184029 i	0.614562 - 0.183738 i	1.27	0.16
5	0	0.749692 - 0.061030 i	0.750694 - 0.061151 i	0.13	0.20
5	1	0.744343 - 0.183647 i	0.750694 - 0.183452 i	0.85	0.11
6	0	0.886039 - 0.061009 i	0.886885 - 0.061096 i	0.10	0.14
6	1	0.881500 - 0.183428 i	0.886885 - 0.183288 i	0.61	0.08

Table 4. Verification of the eikonal limit correspondence: comparison between WKB-computed QNM frequencies (ω_{WKB}) and photon sphere-based predictions (ω_{PS}) for increasing angular quantum number l (fundamental mode $n = 0$). The relative percentage differences $\Delta_R\%$ and $\Delta_I\%$ demonstrate the convergence to the eikonal limit prediction as l increases. Parameters: $a = 0.2$, $A = 1$, $B = 10^{-5}$, $\beta = 0.8$, and $Q = 0.5$.

| l	ω_{WKB}	ω_{PS}	$\Delta_R\%$	$\Delta_I\%$
1	0.203417 - 0.062029 i	0.136327 - 0.060958 i	32.98	1.727
10	1.43138 - 0.060978 i	1.36327 - 0.060958 i	4.759	0.03223
100	13.7009 - 0.060958 i	13.6327 - 0.060958 i	0.4975	3.51×10^{-4}
300	40.9663 - 0.060958 i	40.8981 - 0.060958 i	0.1664	3.926×10^{-5}
500	68.2317 - 0.060958 i	68.1635 - 0.060958 i	0.0999	1.415×10^{-5}
10^3	136.3952 - 0.060958 i	136.327 - 0.060958 i	5.00×10^{-2}	3.542×10^{-6}
10^4	1363.339 - 0.060958 i	1363.27 - 0.060958 i	5.00×10^{-3}	3.545×10^{-8}
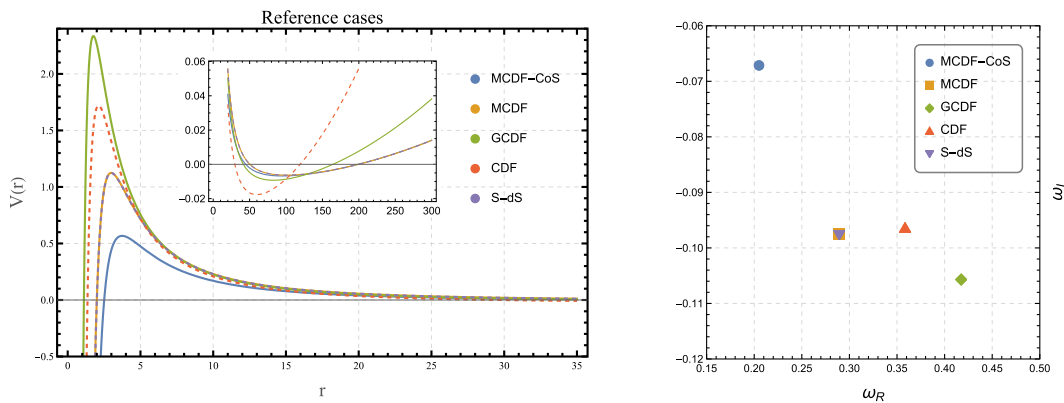
Fig. 4. (color online) Effective potentials (left) and corresponding fundamental ($n = 0$, $l = 1$) QNM frequencies (right) for the reference models. The model parameters are presented in Table 1.

and $|\text{Im}(\omega)|$, leading to lower-frequency and longer-lived ringdown signals as a result of modifications in the spacetime geometry.

The MCDF parameters manifest more nuanced influ-

ences compared with the string cloud contribution (Table 2, Fig. 5). While the MCDF intensity parameter Q and the polytropic index β exhibit negligible impact across their physical ranges, the equation of state parameters A and B
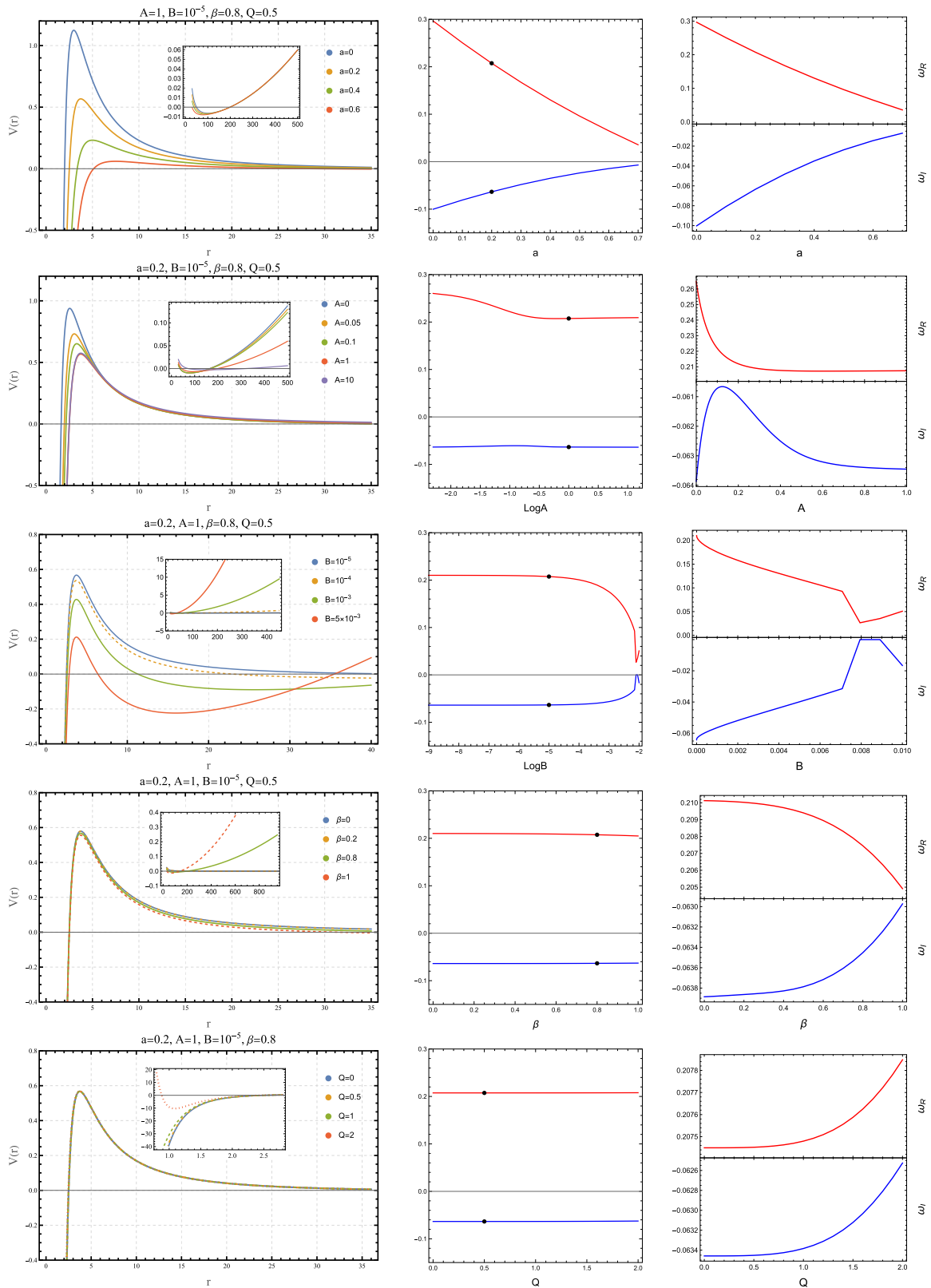
Fig. 5. (color online) Evolution of the fundamental ($n = 0$, $l = 1$) QNMs under parameter variation. From left to right: modifications to the effective potential $V(r)$; the resulting frequency shifts presented on a fixed scale; and the same data on optimized scales to resolve detailed behaviors. The black dot in each panel indicates the reference MCDF-CoS configuration ($a = 0.2$, $A = 1$, $B = 10^{-5}$, $\beta = 0.8$, and $Q = 0.5$).
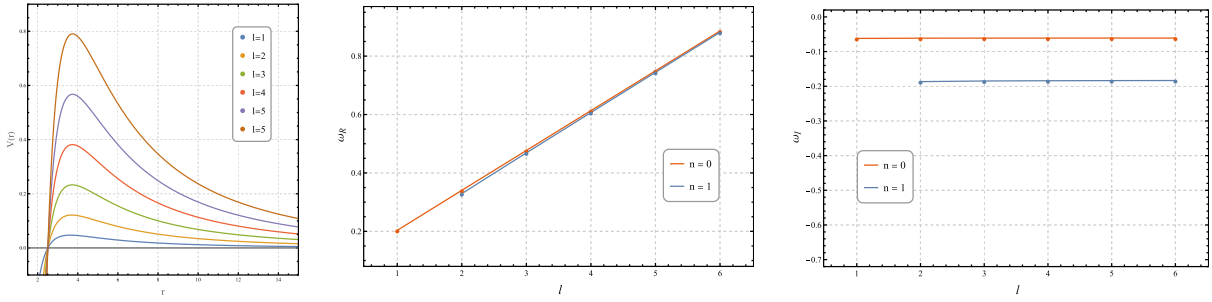
Fig. 6. (color online) Dependence of QNM frequencies on the angular quantum number l and overtone number n for the reference black hole configuration: $a = 0.2$, $A = 1$, $B = 10^{-5}$, $\beta = 0.8$, $Q = 0.5$

demonstrate significant, albeit distinct, modifications, particularly at boundary values. As A increases from its minimum allowed value, $\mathrm{Re}(\omega)$ undergoes an initial rapid decrease followed by convergence to a nearly constant value, with only marginal subsequent variation. Concurrently, $|\mathrm{Im}(\omega)|$ displays a more constrained evolution within a narrow range, characterized by an initial decline succeeded by a slight enhancement before saturation. In contrast, increasing B produces a monotonic suppression of both oscillation frequency and damping rate—initially gradual, then accelerating, with a distinct upturn near the maximum allowed value of B, ensuring the stability of the quasinormal modes by maintaining a positive oscillation frequency and a negative damping rate.

These spectral characteristics directly correspond to the modifications of the effective potential barrier governing wave propagation. The parameters that enhance the potential barrier height (diminished a or B) correspondingly increase $\mathrm{Re}(\omega)$ through a stronger spatial confinement of wave modes. Conversely, the parameters that broaden the potential barrier (enhanced a) reduce $|\mathrm{Im}(\omega)|$ by extending the interaction region and diminishing wave dissipation. The observed parameter-specific behavior near extremal values reveals a remarkable spatial decoupling: A predominantly modulates physics in the near-horizon region, whereas B governs modifications in the cosmological horizon domain. This spatial segregation underscores a fundamental correspondence between the MCDF equation of state parameters and the characteristic scales of the black hole spacetime, reflecting how the linear pressure component (A) and generalized Chaplygin term (B) dominate gravitational interactions in distinct regimes—the former influencing local strong-field dynamics and the latter controlling global cosmological evolution.

The overtone structure presented in Table 3 and Fig. 6 compares the fundamental mode ($n = 0$) with the first overtone ($n = 1$). Consistent with generic black hole behavior, the first overtone exhibits a larger $|\mathrm{Im}(\omega)|$ compared with the fundamental mode, indicating a faster decay rate. For fundamental modes, $|\mathrm{Im}(\omega)|$ decreases and asymptotes with increasing l, whereas $\mathrm{Re}(\omega)$ grows ap-

proximately linearly.

The eikonal limit verification (Table 4) demonstrates the systematic convergence of WKB-computed frequencies ω_{WKB} to the geometric prediction ω_{PS}, with relative errors $\Delta_R\%$ and $\Delta_I\%$ decreasing with l. This confirms the photon sphere/QNM correspondence and underscores the fundamental wave-geometry relationship.

Throughout our analysis, the third-order WKB and Pöschl-Teller methods show excellent agreement for the fundamental modes ($n = 0$), validating our computational approach in this regime. However, the growing relative error observed for $n = 1$ (as shown in Table 3) underscores the necessity for employing higher-precision numerical techniques, such as the continued-fraction method, should a detailed investigation of the higher-overtone spectrum be required in future studies.

V. GREYBODY FACTORS

GBFs quantify the transmission probability of Hawking radiation through the potential barrier to distant observers, crucially influencing the semi-classical evaporation process and observable radiation spectrum.

We consider massless scalar wave scattering governed by Eq. (33) but with scattering boundary conditions

$$\Psi \sim T e^{-\mathrm{i}\omega r_*} \quad (r_* \to -\infty), \tag{42}$$

$$\Psi \sim e^{-\mathrm{i}\omega r_*} + R e^{\mathrm{i}\omega r_*} \quad (r_* \to +\infty), \tag{43}$$

where T and R are the transmission and reflection coefficients, respectively, for real frequency ω. The GBF is defined as $\Gamma_l(\omega) = |T|^2 = 1 - |R|^2$.

We compute GBFs using the third-order WKB approximation [54, 97], which provides the semi-analytical formula

$$\Gamma_l(\omega) = \frac{1}{1 + \exp[2\pi\mathrm{i}\mathcal{K}(\omega)]}, \tag{44}$$

where $\mathcal{K}(\omega)$ is identical to the QNM function (Eq. (38))

but evaluated for real ω. This yields smooth transitions from total reflection ($\Gamma_l \approx 0$) to near-complete transmission ($\Gamma_l \approx 1$) as ω surpasses the potential barrier height.

A.　Eikonal limit connection

In the eikonal limit ($l \gg 1$), a profound correspondence emerges between GBFs, QNMs, and the geometric properties of the photon sphere [43, 53, 101]. This relationship originates from the wave-optic equivalence principle in high-frequency regimes, where wave scattering is governed by the underlying null geodesic structure.

For massless scalar perturbations, the GBF can be expressed in terms of the QNM frequencies through the higher-order correspondence relation developed in Ref. [53]. Utilizing the third-order WKB expansion, the exponent function $-i\mathcal{K}(\omega)$ in the GBF formula (44) is given by

$$-i\mathcal{K}(\omega) = -\frac{\omega^2 - \mathrm{Re}(\omega_0)^2}{4\mathrm{Re}(\omega_0)\mathrm{Im}(\omega_0)} + \Delta_{\mathrm{HO}}(\omega, \omega_0, \omega_1). \qquad (45)$$

Here, ω_0 and ω_1 denote the frequencies of the fundamental mode and first overtone, respectively. The higher-order correction term Δ_{HO}, which accounts for the anharmonicity of the effective potential, is explicitly defined in Ref. [53] (see Eq. (4.3) therein). This higher-order formulation significantly improves accuracy compared with the leading-order approximation, particularly in regimes where the potential deviates from a simple barrier shape.

Employing the eikonal QNM approximation (41) for fundamental modes yields

$$\omega_0 \approx \Omega_{\mathrm{ps}} l - i\frac{|\lambda|}{2}, \qquad (46)$$

with Ω_{ps} and λ given by Eqs. (18) and (19), respectively, which leads to the geometric optics-based expression for

the GBF [101]

$$\Gamma_l(\omega) \approx \frac{1}{1 + \exp\left[-2\pi\left(\frac{\omega - \Omega_{\mathrm{ps}} l}{|\lambda|}\right)\right]}. \qquad (47)$$

A notable observation is that, while the higher-order QNM-GBF correspondence introduced in Eq. (45) demonstrates excellent numerical agreement across the parameter space (Fig. 7), the shadow-GBF relation in Eq. (47) exhibits more pronounced discrepancies. This enhanced sensitivity likely originates from the exponential amplification of small deviations between the actual QNM real part and its geometric optics approximation ($\mathrm{Re}(\omega_0) - \Omega_{\mathrm{ps}} l$) within the GBF expression. Nevertheless, both formulations consistently underscore the fundamental role of photon sphere geometry in governing wave scattering dynamics. Crucially, our analysis highlights a regime-dependent behavior in achieving this agreement: the inclusion of the higher-order correction term Δ_{HO} is essential for low angular momentum modes (e.g., $l = 1, 10$) where the effective potential is anharmonic, whereas the leading-order approximation naturally converges to the exact result in the eikonal limit (e.g., $l = 100$) as the potential barrier becomes harmonic.

B.　GBF results and discussion

The GBF spectrum $\Gamma_l(\omega)$ for MCDF-CoS black holes exhibits systematic dependencies on both angular momentum and spacetime parameters, with the transition frequency and profile sharpness serving as sensitive probes of the underlying geometry (Fig. 8).

Angular momentum dependence reveals that higher multipole numbers shift transmission thresholds to higher frequencies while simultaneously sharpening the transition profiles. For the reference configuration ($a = 0.2$, $A = 1$, $B = 10^{-5}$, $\beta = 0.8$, and $Q = 0.5$), the $l = 1$ mode ini-
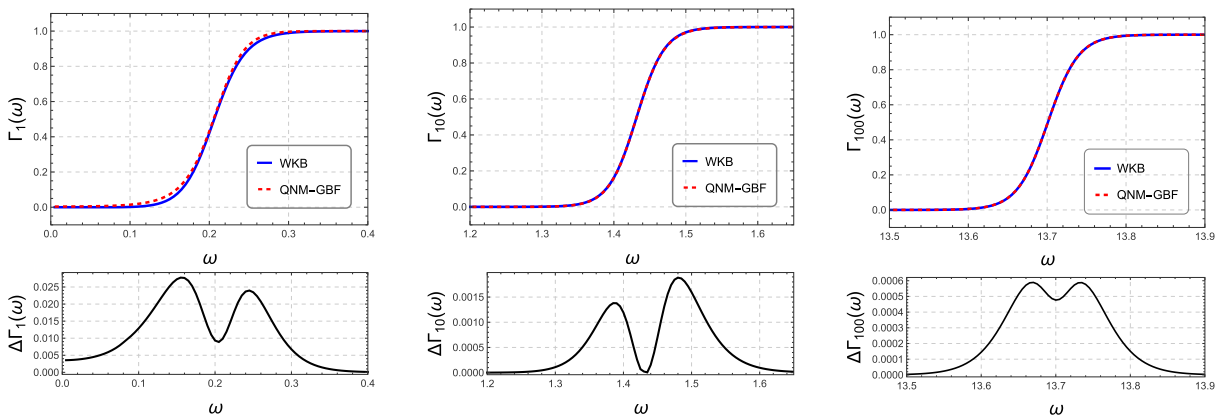

Fig. 7.　(color online) Comparison of GBFs computed via the WKB method and the QNM correspondence. The left and center panels (l=1.10) utilize the higher-order relation [Eq. (45)] including overtone corrections, demonstrating significant improvement in accuracy. The right panel (l=100) retains the leading-order approximation, which remains asymptotically exact in the eikonal limit.
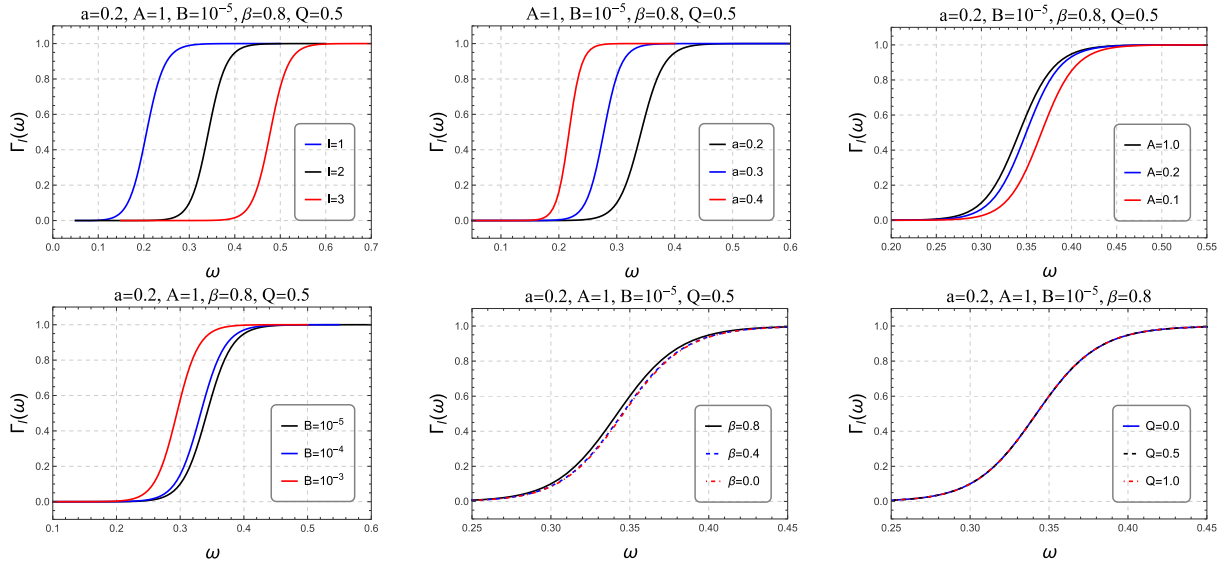
Fig. 8. (color online) Dependence of the GBF spectrum $\Gamma_l(\omega)$ for MCDF-CoS black holes on the multipole number l (first panel) and on spacetime parameters (subsequent panels where we have set $l = 2$).

tiates significant transmission around $\omega \approx 0.1$, whereas the $l = 3$ mode remains substantially suppressed until $\omega \approx 0.3$. This behavior is consistent with the increased potential barriers encountered by higher angular momentum states.

Among the spacetime parameters, the CoS intensity a exerts the most pronounced influence on the GBF spectrum. Increasing a from 0.2 to 0.4 substantially lowers the transmission threshold —shifting the 50% transmission point from $\omega \approx 0.25$ to $\omega \approx 0.15$ for $l = 2$—while concurrently broadening the transition region. This modification reflects the softening of the effective potential barrier induced by the enhanced string cloud density.

The MCDF parameters A and B display distinctive modification patterns to the transmission spectrum, each governed by separate physical mechanisms. Parameter B dominates near its maximum allowed value, where the intensified negative pressure component effectively lowers the potential barrier, substantially enhancing low-frequency transmission. Similarly, parameter A produces its most significant effects at minimal values, where reduced fluid stiffness alters the potential profile, effectively enhancing the tunneling probability for low-frequency waves. This regime-dependent behavior underscores their different roles in the equation of state. In contrast, parameters β and Q exhibit negligible impact on the GBF spectrum across their physically allowed ranges, indicating their minimal influence on the scattering dynamics.

These systematic trends maintain consistent correlations with corresponding modifications in both the effective potential and QNM spectra discussed previously. The enhanced low-frequency transmission for larger a values suggests potentially observable modifications to the

Hawking radiation spectrum. The identified parameter sensitivities demonstrate that future high-precision measurements could constrain the string cloud intensity and key MCDF parameters (A and B), whereas β and Q remain challenging to probe through GBF measurements alone.

VI. SUMMARY AND CONCLUSIONS

In this comprehensive study, we systematically investigated the gravitational properties of static, spherically symmetric black holes immersed in an MCDF and a CoS. By focusing on three key theoretical signatures—the black hole shadow, QNMs, and GBFs—we elucidated how these exotic environmental components collectively modify the fundamental characteristics and observable manifestations of black holes.

The spacetime geometry, characterized by the metric function in Eq. (1), incorporates the MCDF through a hypergeometric function contribution $G(r)$ and the CoS via the parameter a. This framework encompasses several limiting cases and exhibits asymptotically de Sitter behavior, with the existence of black hole solutions imposing specific bounds on the parameter space.

Our analysis reveals a coherent and consistent picture across all three phenomena. The CoS parameter a emerges as the dominant factor, whose increase significantly increases the shadow radius, reduces both the oscillation frequency and damping rate of QNMs (leading to longer-lived ringdown signals), and substantially enhances low-frequency transmission in GBFs. This universal trend underscores the profound impact of the string cloud in globally softening the effective potential and altering the underlying spacetime geometry.

The influence of the MCDF parameters is more selective and reveals a nuanced hierarchy. The optical shadow is primarily affected at parameter extremes, where increasing A increases the shadow radius, whereas increasing B reduces it. The QNM spectrum unveils a remarkable spatial decoupling: parameter A, associated with the linear pressure component, predominantly modulates the near-horizon physics, whereas parameter B, linked to the generalized Chaplygin term, governs the cosmological horizon domain. This spatial segregation is further reflected in the GBFs, where both parameters produce significant but regime-dependent effects: parameter B dominates near its maximum value by lowering the potential barrier, whereas parameter A exerts its strongest influence at minimal values by altering the potential profile to enhance low-frequency tunneling. Notably, the parameters Q and β exhibit negligible impact across all observational channels, indicating their subdominant role in the gravitational phenomenology studied here.

Beyond these parameter dependencies, our study highlights fundamental physical connections. The shadow appearance under different accretion flows demonstrates how accretion dynamics (e.g., Doppler beaming in the infalling model) shape the morphology of the bright emission ring, independent of the shadow size itself—a purely geometric attribute. Furthermore, the verification of the eikonal limit firmly establishes the fundamental correspondence between the photon sphere (a geometric entity), QNM spectrum (a wave entity), and GBFs, thereby presenting a unified description of black hole dynamics that bridges wave and geometric optics.

Our findings suggest several promising avenues for future studies. The identified parameter dependencies could inform efforts to constrain exotic matter components, particularly through shadow observations and QNM detections with current and next-generation instruments. The GBF results, while more theoretical at present, provide important insights into the scattering properties of black holes and would become directly relevant should evidence of Hawking radiation or other quantum emissions be discovered. Extending this analysis to rotating black holes would greatly enhance its astrophysical relevance. Additionally, investigating electromagnetic perturbations and thermodynamic implications could provide a more complete characterization of these complex systems.

In conclusion, the MCDF-CoS black hole framework provides a rich theoretical laboratory for probing how exotic matter and extended structures modify fundamental black hole properties. The systematic dependencies and unified relationships we have identified not only deepen the theoretical understanding but also provide concrete, multi-faceted predictions for future astronomical observations aimed at deciphering the intricate environments surrounding these fascinating objects.

References

[1] K. Akiyama *et al*. (Event Horizon Telescope Collaboration), Astrophys. J. Lett. **875**, L1 (2019)

[2] K. Akiyama *et al*. (Event Horizon Telescope Collaboration), Astrophys. J. Lett. **930**, L12 (2022)

[3] B. P. Abbott *et al*. (LIGO Scientific and Virgo Collaborations), Phys. Rev. Lett. **116**, 061102 (2016)

[4] V. Cardoso and P. Pani, Nature Astron. **1**, 586 (2017), arXiv: 1709.01525[gr-qc]

[5] V. Perlick and O. Y. Tsupko, Phys. Rept. **947**, 1 (2022), arXiv: 2105.07101[gr-qc]

[6] P. Kocherlakota and L. Rezzolla, Mon. Not. Roy. Astron. Soc. **513**, 1229 (2022), arXiv: 2201.05641[gr-qc]

[7] Y. Hou, Z. Zhang, H. Yan *et al*., Phys. Rev. D **106**, 064058 (2022), arXiv: 2206.13744[gr-qc]

[8] Y. Hou, J. Huang, M. Guo *et al*., Astrophys. J. Lett. **988**, L51 (2025), arXiv: 2409.07248[gr-qc]

[9] M. Guo, N. A. Obers, and H. Yan, Phys. Rev. D **98**, 084063 (2018), arXiv: 1806.05249[gr-qc]

[10] P.-C. Li, M. Guo, and B. Chen, Phys. Rev. D **101**, 084041 (2020a), arXiv: 2001.04231[gr-qc]

[11] Z. Hu, Z. Zhong, P.-C. Li *et al*., Phys. Rev. D **103**, 044057 (2021), arXiv: 2012.07022[gr-qc]

[12] Z. Zhao, Z.-Y. Fan, X. Wang *et al*., (2025), arXiv: 2510.27409[astro-ph.HE]

[13] Z. Y. Fan, F. Zhou, Y. Li *et al*., Phys. Rev. D **111**, 064067 (2025), arXiv: 2411.19491[astro-ph.HE]

[14] J.-Y. Gui, K.-J. He, H. Ye *et al*., Front. Phys. (Beijing) **20**, 25202 (2025), arXiv: 2407.09069[hep-th]

[15] X.-X. Zeng, H.-Q. Zhang, and H. Zhang, Eur. Phys. J. C **80**, 872 (2020), arXiv: 2004.12074[gr-qc]

[16] X.-X. Zeng, G.-P. Li, and K.-J. He, Nucl. Phys. B **974**, 115639 (2022), arXiv: 2106.14478[hep-th]

[17] X.-X. Zeng, K.-J. He, J. Pu *et al*., Eur. Phys. J. C **83**, 897 (2023a), arXiv: 2302.03692[gr-qc]

[18] K.-J. He, H. Ye, X.-X. Zeng *et al*., Chin. Phys. C **49**, 125103 (2025a), arXiv: 2502.08388[gr-qc]

[19] K. J. He, G. P. Li, C. Y. Yang *et al*.,,JCAP **10**, 003 (2025), arXiv: 2502.16623[gr-qc]

[20] X. Wang, Z. Zhao, X.-X. Zeng *et al*., Phys. Rev. D **111**, 084054 (2025), arXiv: 2501.08287[gr-qc]

[21] E. Battista, Phys. Rev. D **109**, 026004 (2024), arXiv: 2312.00450[gr-qc]

[22] Z.-L. Wang and E. Battista, Eur. Phys. J. C **85**, 304 (2025), arXiv: 2501.14516[gr-qc]

[23] N. Tsukamoto, Z. Li, and C. Bambi,JCAP **06**, 043 (2014), arXiv: 1403.0371[gr-qc]

[24] N. Tsukamoto, Phys. Rev. D **97**, 064021 (2018), arXiv: 1708.07427[gr-qc]

[25] S. B. Chen and J. L. Jing, Class. Quant. Grav. **22**, 4651 (2005), arXiv: gr-qc/0511085

[26] R. A. Konoplya, Phys. Lett. B **795**, 1 (2019), arXiv: 1905.00064[gr-qc]

[27] X.-X. Zeng, H. Ye, K.-J. He *et al*., Eur. Phys. J. C **85**, 1211 (2025a), arXiv: 2507.11583[gr-qc]

[28] X.-X. Zeng, M. I. Aslam, and R. Saleem, Eur. Phys. J. C **83**, 129 (2023b), arXiv: 2208.06246[gr-qc]

[29] X.-X. Zeng, C.-Y. Yang, M. I. Aslam *et al.*,,JCAP **08**, 066 (2025), arXiv: 2505.07063[gr-qc]

[30] Y. F. Chen, R. Ding, Y. X. Liu *et al.*, Phys. Rev. Lett. **135**, 121001 (2025), arXiv: 2404.16673[hep-ph]

[31] E. Berti, V. Cardoso, and A. O. Starinets, Class. Quant. Grav. **26**, 163001 (2009), arXiv: 0905.2975[gr-qc]

[32] R. A. Konoplya and A. Zhidenko, Rev. Mod. Phys. **83**, 793 (2011), arXiv: 1102.4014[gr-qc]

[33] S. A. Teukolsky, Astrophys. J. **185**, 635 (1973)

[34] W. H. Press and S. A. Teukolsky, Astrophys. J. **185**, 649 (1973)

[35] H.-P. Nollert, Class. Quant. Grav. **16**, R159 (1999)

[36] C. Chen, J. Jing, Z. Cao *et al.*, Phys. Rev. D **112**, 103036 (2025b), arXiv: 2506.14635[gr-qc]

[37] Y. Guo, H. Xie, and Y.-G. Miao, Phys. Lett. B **855**, 138801 (2024), arXiv: 2402.10406[gr-qc]

[38] Y. Liu, B. Mu, J. Tao *et al.*, Nucl. Phys. B **1010**, 116787 (2025), arXiv: 2409.20333[gr-qc]

[39] A. Zhidenko, Class. Quant. Grav. **21**, 273 (2004), arXiv: gr-qc/0307012

[40] S. W. Hawking, Commun. Math. Phys. **43**, 199 (1975)

[41] Y. Decanini, G. Esposito-Farese, and A. Folacci, Phys. Rev. D **83**, 044032 (2011), arXiv: 1101.0781[gr-qc]

[42] C.-Y. Zhang, P.-C. Li, and M. Guo, Eur. Phys. J. C **80**, 874 (2020), arXiv: 2003.13068[hep-th]

[43] V. Cardoso, A. S. Miranda, E. Berti *et al.*, Phys. Rev. D **79**, 064016 (2009), arXiv: 0812.1806[hep-th]

[44] H. Yang, D. A. Nichols, F. Zhang *et al.*, Phys. Rev. D **86**, 104006 (2012), arXiv: 1207.4253[gr-qc]

[45] K. Jusufi, Phys. Rev. D **101**, 084055 (2020), arXiv: 1912.13320[gr-qc]

[46] P.-C. Li, T.-C. Lee, M. Guo *et al.*, Phys. Rev. D **104**, 084044 (2021), arXiv: 2105.14268[gr-qc]

[47] J. A. V. Campos, M. A. Anacleto, F. A. Brito *et al.*, Sci. Rep. **12**, 8516 (2022), arXiv: 2103.10659[hep-th]

[48] R. A. Konoplya, A. Khrabustovskyi, J. Kříž *et al.*,JCAP **04**, 062 (年), arXiv: 2501.16134[gr-qc]

[49] S.-H. Xiong, Y.-Z. Li, X.-M. Kuang *et al.*, Eur. Phys. J. C **85**, 1143 (2025), arXiv: 2508.03270[gr-qc]

[50] N. Oshita, Phys. Rev. D **104**, 124032 (2021), arXiv: 2109.09757[gr-qc]

[51] R. F. Rosato, K. Destounis, and P. Pani, Phys. Rev. D **110**, L121501 (2024), arXiv: 2406.01692[gr-qc]

[52] N. Oshita, K. Takahashi, and S. Mukohyama, Phys. Rev. D **110**, 084070 (2024), arXiv: 2406.04525[gr-qc]

[53] R. A. Konoplya and A. Zhidenko, JCAP **09**, 068 (2024), arXiv: 2406.11694[gr-qc]

[54] R. A. Konoplya, A. Zhidenko, and A. F. Zinhailo, Class. Quant. Grav. **36**, 155002 (2019), arXiv: 1904.10333[gr-qc]

[55] Y. Guo, C. Lan, and Y.-G. Miao, Phys. Rev. D **106**, 124052 (2022), arXiv: 2201.02971[gr-qc]

[56] Y. Guo and Y.-G. Miao, Nucl. Phys. B **983**, 115938 (2022), arXiv: 2112.01747[gr-qc]

[57] Y. Guo and Y.-G. Miao, Phys. Rev. D **102**, 084057 (2020), arXiv: 2007.08227[hep-th]

[58] Q.-L. Shi, R. Wang, W. Xiong *et al.*, (2025), arXiv: 2506.16217[gr-qc]

[59] A. G. Riess *et al.* (Supernova Search Team), Astron. J. **116**, 1009 (1998), arXiv: astro-ph/9805201

[60] S. Perlmutter *et al.* (Supernova Cosmology Project Collaboration), Astrophys. J. **517**, 565 (1999), arXiv:

[61] L.-M. Wang, R. R. Caldwell, J. P. Ostriker *et al.*, Astrophys. J. **530**, 17 (2000), arXiv: astro-ph/9901388

[62] N. A. Bahcall, J. P. Ostriker, S. Perlmutter *et al.*, Science **284**, 1481 (1999), arXiv: astro-ph/9906463

[63] V. V. Kiselev, Class. Quant. Grav. **20**, 1187 (2003), arXiv: gr-qc/0210040

[64] T. Lacroix and J. Silk, Astron. Astrophys. **554**, A36 (2013), arXiv: 1211.4861[astro-ph.GA]

[65] S. U. Khan and J. Ren, Phys. Dark Univ. **30**, 100644 (2020), arXiv: 2006.11289[gr-qc]

[66] X.-X. Zeng and H.-Q. Zhang, Eur. Phys. J. C **80**, 1058 (2020), arXiv: 2007.06333[gr-qc]

[67] A. He, J. Tao, Y. Xue *et al.*, Chin. Phys. C **46**, 065102 (2022), arXiv: 2109.13807[gr-qc]

[68] D. J. Gogoi, N. Heidari, J. Kriz *et al.*, Fortsch. Phys. **72**, 2300245 (2024), arXiv: 2307.09976[gr-qc]

[69] G. Fatima, S. Shaukat, F. Javed *et al.*, Phys. Dark Univ. **45**, 101521 (2024)

[70] B. Hamil and B. C. Lütfüoğlu, Fortsch. Phys. **73**, 2400105 (2025a), arXiv: 2406.02109[gr-qc]

[71] A. Kamenshchik, U. Moschella, and V. Pasquier, Phys. Lett. B **511**, 265 (2001), arXiv: gr-qc/0103004[gr-qc]

[72] N. Bilic, G. B. Tupper, and R. D. Viollier, Phys. Lett. B **535**, 17 (2002), arXiv: astro-ph/0111325[astro-ph]

[73] M. C. Bento, O. Bertolami, and A. A. Sen, Phys. Rev. D **66**, 043507 (2002), arXiv: gr-qc/0202064[gr-qc]

[74] C.-G. Park, J.-c. Hwang, J. Park *et al.*, Phys. Rev. D **81**, 063532 (2010), arXiv: 0910.4202[astro-ph.CO]

[75] N. Aggarwal, A. Pourmand, F. Shojai *et al.*, Annals Phys. **483**, 170266 (2025), arXiv: 2510.12472[gr-qc]

[76] N. Ogawa, Phys. Rev. D **62**, 085023 (2000), arXiv: hep-th/0003288

[77] M. Bordemann and J. Hoppe, Phys. Lett. B **317**, 315 (1993), arXiv: hep-th/9307036

[78] R. Jackiw and A. P. Polychronakos, Phys. Rev. D **62**, 085019 (2000), arXiv: hep-th/0004083

[79] X.-Q. Li, B. Chen, and L.-l. Xing, Eur. Phys. J. Plus **135**, 175 (2020b), arXiv: 1905.08156[gr-qc]

[80] X.-Q. Li, B. Chen, and L.-L. Xing, Eur. Phys. J. Plus **137**, 1167 (2022a), arXiv: 1908.09827[gr-qc]

[81] X.-Q. Li, B. Chen, and L.-L. Xing, Annals Phys. **446**, 169125 (2022b)

[82] X.-Q. Li, H.-P. Yan, L.-L. Xing *et al.*, Phys. Rev. D **107**, 104055 (2023), arXiv: 2305.03028[gr-qc]

[83] X.-Q. Li, H.-P. Yan, X.-J. Yue *et al.*,JCAP **05**, 048 (2024), arXiv: 2401.18066[gr-qc]

[84] X. Q. Li, Y. Kim, B. H. Lee *et al.*, Chin. Phys. C **49**, 105104 (2025), arXiv: 2505.12077[gr-qc]

[85] Y. Sekhmani, D. J. Gogoi, S. K. Maurya *et al.*, JHEAp **45**, 200 (2025)

[86] R. Bécar, P. A. González, E. Papantonopoulos *et al.*,JCAP **06**, 061 (2024), arXiv: 2403.11306[gr-qc]

[87] S. S. Bohra, (2025), arXiv: 2509.14064[gr-qc]

[88] P. S. Letelier, Phys. Rev. D **20**, 1294 (1979)

[89] B. Hamil and B. C. Lütfüoğlu, Chin. Phys. C **49**, 025107 (2025), arXiv: 2410.09551[gr-qc]

[90] M. Sadeghi and H. Ranjbari, Class. Quant. Grav. **36**, 205012 (2019), arXiv: 1905.12856[hep-th]

[91] M. Sadeghi, Mod. Phys. Lett. A **35**, 2050330 (2020), arXiv: 2001.01171[hep-th]

[92] M. Sadeghi and F. Rahmani, Int. J. Mod. Phys. A **38**, 2350102 (2023), arXiv: 2301.12411[hep-th]

[93] M. Jaroszynski and A. Kurpiewski, Astron. Astrophys. **326**, 419 (1997), arXiv: astro-ph/9705044

[94] C. Bambi, Phys. Rev. D **87**, 107501 (2013), arXiv: 1304.5691[gr-qc]

[95] A. M. Bauer, A. Cárdenas-Avendaño, C. F. Gammie *et al*., Astrophys. J. **925**, 119 (2022), arXiv: 2111.02178[gr-qc]

[96] B. F. Schutz and C. M. Will, Astrophys. J. Lett. **291**, L33 (1985)

[97] S. Iyer and C. M. Will, Phys. Rev. D **35**, 3621 (1987)

[98] R. A. Konoplya, Phys. Rev. D **68**, 024018 (2003), arXiv: gr-qc/0303052[gr-qc]

[99] V. Ferrari and B. Mashhoon, Phys. Rev. D **30**, 295 (1984)

[100] B. Mashhoon, Phys. Rev. D **31**, 290 (1985)

[101] D. Pedrotti and M. Calzà, Phys. Rev. D **111**, 124056 (2025), arXiv: 2504.01909[gr-qc]